

pubs.acs.org/crystal Article

# Composition Engineering and Crystal Growth of High-Entropy Rare-Earth Monoclinic Aluminates

Yauhen Tratsiak,\* Bethany Claes, Charles L. Melcher, and Mariya Zhuravleva



**Cite This:** https://doi.org/10.1021/acs.cgd.4c00633



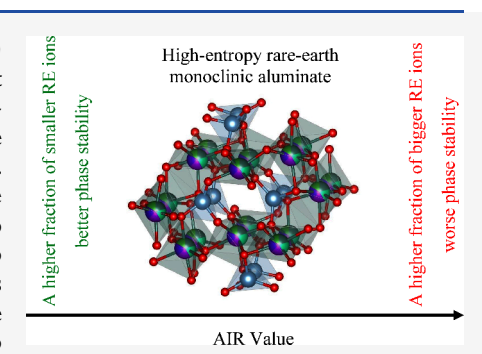
**ACCESS** I

Metrics & More

Article Recommendations

SI Supporting Information

ABSTRACT: We generated high-entropy (HE) compositions of rare-earth (RE) monoclinic aluminates using a combinatorial approach, grew crystals from the melt using the micropulling down method, and investigated phase formation, microstructure, and elemental segregation. All RE elements, except for *Pm* and Tm, were used to generate RE<sub>4</sub>Al<sub>2</sub>O<sub>9</sub> compounds of five RE elements taken in equimolar ratios. The distribution of HE formulations was demonstrated as a function of the average ionic radii (AIR). The compositions were grouped based on their AIR that is equal to those of RE ions in single-rare-earth compounds: Y<sub>4</sub>Al<sub>2</sub>O<sub>9</sub> (Y group), Tb<sub>4</sub>Al<sub>2</sub>O<sub>9</sub> (Tb group), Gd<sub>4</sub>Al<sub>2</sub>O<sub>9</sub> (Gd group), and Nd<sub>4</sub>Al<sub>2</sub>O<sub>9</sub> (Nd group). Single monoclinic phases and uniform microstructures were observed in the Y group. Dot-, line-, and core-like inclusions of the secondary REAlO<sub>3</sub> perovskite phase were found in crystals of the Tb group and the Gd group in scanning electron micrographs. The concentration of the



secondary phase increased with the fraction of bigger RE elements, such as La, Ce, Pr, Nd, and Sm in the HE formulation, as confirmed by X-ray diffraction. Incongruent melt solidification was found for compounds of the Nd group. Our results demonstrated that the stability of the monoclinic phase decreased with the AIR value in the sequence of the Y group, Tb group, Gd group, and Nd group, similar to their single-rare-earth compounds. Minor random variations in cell parameters between the seed and tail sides were found in crystals from the Y group, Tb group, and Gd group, indicating no pronounced elemental segregation. Based on the ionic radii of RE elements and their fraction in the HE formulation, recommendations were given on how to minimize the secondary phase.

# **■ INTRODUCTION**

The high-entropy (HE) approach, comprising five or more equiatomic elements mixed into one crystallographic site, has become a popular way to develop new and improve the properties of existing oxide, halide, and alloy-based materials. <sup>1–7</sup> Different from traditional methods that focus on single-component composition tuning, structure, or morphology control, the HE approach focuses on introducing compositional disorder. This can provide a few benefits: (i) solid solutions of many elements tend to be more stable because of large configurational entropy; <sup>8–11</sup> (ii) the multicomponent composition leads to an improvement of current or contribution of new properties to the materials. <sup>12</sup> The HE approach provides an incredibly large number of possible compositional combinations, while only a small fraction has been investigated.

Rare-earth (RE) aluminates are a large group of compounds with multiple structures and flexible latices, which leads to high interest in their investigation and practical applications. RE aluminates include garnet RE<sub>3</sub>Al<sub>5</sub>O<sub>12</sub>, perovskite REAlO<sub>3</sub>, and monoclinic RE<sub>4</sub>Al<sub>2</sub>O<sub>9</sub> (or REAM) families. Multirare-earth garnets and perovskites were studied,  $^{2,5,7,14-17}_{-17}$  but the monoclinic compounds in single-rare-earth (single RE cation in the formulation) and multirare-earth (or HE) forms are the least investigated group among the RE aluminates. This is a

result of limited phase stability for some single-rare-earth REAM $^{18}$  and phase transition at cooling,  $^{19-22}$  which makes crystal growth from the melt challenging.

Only a few reports are available for the HE rare-earth monoclinic aluminates. <sup>14,19</sup> The HE rare-earth monoclinic aluminates, as their single-component counterparts, can be used in various fields. They can be used as hosts for different optically active ions such as Ce<sup>3+</sup>, Eu<sup>2+</sup>, Pr<sup>3+</sup>, etc. The combination of specific host elements and dopants can be exploited to reach improved energy transfer between the host and the dopant. It was demonstrated that mixed compounds, such as garnets (which are also rare-earth aluminates), can exhibit better luminescent characteristics compared to their single-component counterparts. <sup>23,24</sup> We can reasonably expect the same effect for the HE RE monoclinic aluminates. The HE rare-earth monoclinic aluminates can be used as promising materials for environmental barrier coatings

Received: May 8, 2024
Revised: September 1, 2024
Accepted: September 3, 2024



demonstrating properties better than the single-rare-earth component counterparts. Superior properties of HE compounds are attributed to lattice distortion and the mass difference of constituent atoms, while the entropy stabilization effect explains the improved phase stability at high temperatures. Thus, the development and investigation of HE rare-earth monoclinic aluminates are important, as this can improve their functional properties and expand the fields of possible applications.

Traditionally, the design of HE compounds is based on experimental approaches and intuition or experience earned during multiple trial experiments. The implementation of various machine-learning models or artificial neural networks has been demonstrated as an effective way to predict some properties of HE materials and can accelerate their development.<sup>25,26</sup> The computational approaches for modeling such systems are comparatively less developed than those for single-component structures due to their significant chemical complexity. Computational methods can also provide some benefits for the design of HE compositions. A combinatorial approach can be used to generate a full list of all possible combinations of elements or their gradients for subsequent filtering or computations based on required parameters.<sup>27–29</sup> The average ionic radius (AIR) is another concept used for HE composition engineering. 29,30 The main idea is to use a combination of cations whose average ionic radius is equal to the ionic radius of the cation in the same sublattice site in a given single-component compound. It has been successfully implemented in the composition design of some HE rare-earth garnets, <sup>7,15,31,32</sup> perovskites, <sup>5,33–36</sup> and monoclinic compounds. <sup>14,19</sup> The synergy between the combinatorial approach and the AIR concept looks interesting and promising for the HE composition engineering of rare-earth aluminates.

Single crystals of HE rare-earth aluminates have some advantages over their ceramic or powder counterparts that make them desirable for the discovery of new functional and structural properties. However, their complex chemical composition poses a challenge to crystal growth. Elemental segregation results in undesired microscopic and macroscopic inhomogeneities or compositional gradients within the crystal volume. Among different crystal growth methods, the micropulling-down (u-PD) provides a few benefits for HE materials. The  $\mu$ -PD method minimizes segregation and promotes an axially homogeneous elemental distribution due to a fast-pulling rate, high thermal gradient, small solidifying volume and crystallization zone, and strong Marangoni convection.  $^{37}$  The  $\mu$ -PD method also allows solidifying of the whole volume of the melt during the growth process, minimizing any residual melt in the crucible. The  $\mu$ -PD method in comparison with the Czochralski and Bridgman methods is ideal for research purposes.<sup>37,38</sup>

Considering the above, the main goals of this work are

- i. Applying both the AIR concept and combinatorial approach for composition engineering and selection of HE rare-earth monoclinic aluminates.
- ii. To grow single crystals using the  $\mu$ -PD method and investigate elemental segregation, phase formation, and microstructure by comparing both seed and tail sides of the crystals.
- iii. To investigate whether the AIR value is responsible for the phase formation.

Four single-rare-earth compounds of RE monoclinic aluminates,  $Y_4Al_2O_9$ ,  $Nd_4Al_2O_9$ ,  $Tb_4Al_2O_9$ , and  $Gd_4Al_2O_9$ , were chosen as model compounds for verification of the AIR concept and combinatorial approach to HE composition formulation. Single-rare-earth  $Y_4Al_2O_9$  was chosen due to its excellent phase stability;  $^{18}$   $Tb_4Al_2O_9$  and  $Gd_4Al_2O_9$  were chosen due to their mean ionic radii values among RE elements.  $^{18}$  These compositions provide a relatively high diversity of possible HE combinations. Three of them,  $Y_4Al_2O_9$ ,  $Tb_4Al_2O_9$ , and  $Gd_4Al_2O_9$ , congruently solidify from the melt.  $^{18}$  The remainder,  $Nd_4Al_2O_9$ , melts incongruently,  $^{18,39}$  and was chosen to investigate whether all HE combinations with the same AIR value as the ionic radius of Nd will have similar solidification behavior.

#### MATERIALS AND METHODS

**HE-Formulation Engineering.** The combinatorial approach was used to generate HE formulations of five rare-earth elements taken in equimolar ratios. Y, La, Ce, Pr, Nd, Sm, Eu, Gd, Tb, Dy, Ho, Er, Yb, and Lu were used as the sets of elements for generating HE combinations. All formulations were generated using the Python package *Itertools* v.8.12.0. The number of unique combinations of k elements formed by the set of n elements can be found with the equation:

$$C_n^k = \frac{n!}{(n-k)!k!}$$

The probability of the occurrence of a specific RE element in a HE formulation was calculated as the ratio of the total number of occurrences of this element in the HE formulations of the given set to the total number of HE formulations in the set.

The  $RE_4Al_2O_9$  system belongs to the P21/c space group (Figure S1). The RE atoms in  $RE_4Al_2O_9$  structure are bonded to oxygen atoms with coordination numbers six and seven, forming the  $REO_6$  and  $REO_7$  polyhedral units, respectively. The ionic radii for Lu, Ho, Nd, and Pr for a coordination number of seven are not listed in the literature; thus, we only considered a coordination number of six when calculating AIR values for selecting HE compositions. The processing of the generated HE combinations (AIR calculations, segmentation of combinations based on their AIR value, etc.) was done using Python 3.10.

Crystal Growth and Sample Preparation. The Ø3 mm cylindrical crystals of HE monoclinic aluminates were grown using the micropulling-down method. A KDN Dai-Ichi Kiden growth station was used with a TR-02001 radiofrequency generator operating at 40-44 kV. The starting materials for single and multicomponent compounds were Y2O3, La2O3, Ce2O3, Pr2O3, Nd<sub>2</sub>O<sub>3</sub>, Sm<sub>2</sub>O<sub>3</sub>, Eu<sub>2</sub>O<sub>3</sub>, Gd<sub>2</sub>O<sub>3</sub>, Tb<sub>2</sub>O<sub>3</sub>, Dy<sub>2</sub>O<sub>3</sub>, Ho<sub>2</sub>O<sub>3</sub>, Lu<sub>2</sub>O<sub>3</sub>, Er<sub>2</sub>O<sub>3</sub>, Yb<sub>2</sub>O<sub>3</sub>, and Al<sub>2</sub>O<sub>3</sub> powders of at least 99.99% purity. All powders were stored inside a desiccator in closed vials to prevent possible contact with ambient moisture. The powders were mixed in the required stoichiometric ratios. The total amount of oxide for each composition was 0.6 g. The powder mixtures were melted by inductive heating of the crucible. A Ø16 mm iridium crucible with an Ø3 mm die and a Ø0.5 mm capillary channel was used as the melt reservoir. An iridium pin was used as a seed to initiate the growth by touching the bottom outlet of the crucible capillary channel and pulling down the melt. The initial pulling rate was 0.05 mm/min and was increased gradually to 0.15 mm/min with a 0.01 mm/min step every two min when the crystal diameter reached the crucible die diameter. The grown crystals were cooled to room temperature over 2 h using a gradual decrease of RF generator power to 0%. Grown crystals were ~12 mm long and 3 mm in diameter. Almost the whole volume of the melt was solidified during the growth, and only a tiny fraction of the material remained in the capillary channel after the growth of some crystals. It should be noted that the amount of powder and growth parameters allowed to complete a growth experiment in 1 day.

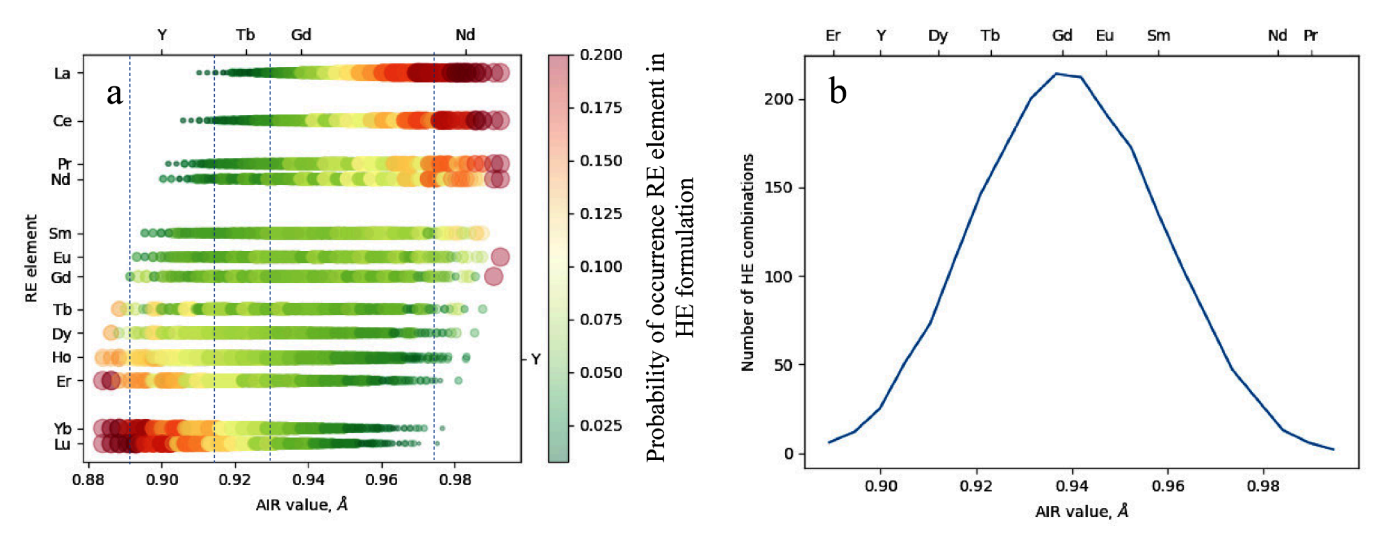


**Figure 1.** (a) Distribution of contribution of RE elements in HE formulations as a function of the AIR value. The size and color of the circle represent the probability of occurrence of the RE element in the HE formulation with a given AIR value. The AIR values corresponding to the Y, Tb, Gd, and Nd groups are listed at the top; (b) distribution of the number of HE combinations for different AIR values. The points on the curve correspond to the Y group, Tb group, Gd group, and Nd group.

After the growth process, all crystals were cut into three equal sections (~0.3 cm long) perpendicular to the growth axis by using a Buehler IsoMet 4000 linear precision saw. The samples were then cleaned in a VWR 50HT sonicator to remove excess crystal bonds, which was used to mount samples during the cutting process. The seed and tail ends of the crystal were both ground using a mortar and pestle for powder X-ray diffraction (XRD) analysis, and the middle section was investigated by using optical microscopy and scanning electron microscopy (SEM).

The list of grown HE compositions with their AIR values, relevance to the single-rare-earth RE<sub>4</sub>Al<sub>2</sub>O<sub>9</sub>, and some measured properties are shown in Table ST1.

**Sample Characterization.** *X-ray Diffraction Measurements.* Powder X-ray diffraction measurements were performed on the seed and tail ends of the REAM crystals ground to powder. The data were collected at room temperature by using a PANalytical Empyrean diffractometer in the Bragg–Brentano geometry with a Cu Kα X-ray source operated at 45 kV and 40 mA. The patterns were used to determine the phase composition and lattice parameters via Rietveld structure refinements performed with the GSAS-II software. The structures of  $Y_4Al_2O_9$  (ICSD #252973),  $Gd_4Al_2O_9$  (ICDD #04–010–3647),  $Tb_4Al_2O_9$  (ICSD #164882), and  $Nd_4Al_2O_4$  (ICSD #249016) were used as references for fitting XRD patterns. The wR value was used for evaluating the quality of the fit. The value did not exceed 8%.

Scanning Electron Microscopy and Energy Dispersive X-ray Spectroscopy Measurements. The Phenom XL scanning electron microscope coupled with energy dispersive X-ray spectroscopy (EDS) was used to investigate microstructure and to analyze elemental composition. The samples were mounted onto a sample holder using carbon tape and loaded in the microscope. The microscope was used in variable-pressure mode (60 Pa) at 15 kV. All SEM images were taken of the crystal cross section along the radial direction with at least 10% overlapping between images for subsequent stitching, which required around 5 separate images at 400× magnification. Stitching of the SEM images was carried out using the OpenCV package functionality. Line scans were done across the entire cross-section of the crystal. Using the EDS functionality, line scans were collected with 32 points on each line for each image, leading to around 160 sample points for the whole cross section. The direction and position of the lines were held the same as those of the SEM images.

Optical Microscopy. Microstructures along crystal cross sections perpendicular to the growth direction, both in seed-side and tail-side, were investigated by using a Leica S6D optical microscope. An LSM-

4000LE-M polarization filter was used to increase the contrast between the crystal and the background. A Leica MC 170HD camera coupled with the ocular lens was used to obtain images. The resulting images were  $2592 \times 1944$  pixels and were cropped further to remove excess background.

# ■ RESULTS AND DISCUSSION

**HE Composition Engineering.** A combinatorial approach and the AIR concept were used to design and select HE combinations for subsequent growth experiments. A list of all possible 2002 combinations of five equimolar rare earth elements was generated by using a combinatorial approach. First, we considered Y, La, Ce, Pr, Nd, Sm, Eu, Gd, Tb, Dy, Ho, Er, Yb, and Lu as the sets of elements for generating combinations. After this, the AIR values were calculated for all generated HE combinations. 43 The distribution of the contribution of RE elements in the HE formulations as a function of the AIR value is shown in Figure 1a. The circles for any given AIR value in the plot represent the RE elements (y-axis) that can be used to compose HE formulations with this AIR value. For clarity of visual presentation, the circle size and color represent the probability of occurrence (contribution) of an RE element in a HE formulation with the AIR value given on the x-axis.

The distribution of the total number of HE combinations for different AIR values is shown in Figure 1b. It depends on the AIR value and is close to the normal distribution. It is consistent with uniform RE ionic radii distribution and equimolar fractions of RE in the HE formulations. A higher number of HE combinations can be generated for the mean AIR values that are located in the middle of the RE series close to the ionic radii of Tb, Gd, and Eu. The range of AIR values for five-component equimolar formulations is from 0.884 to 0.995 Å, which is narrower than the range of ionic radii of the RE elements from Lu to La. Five-RE equimolar HE combinations with AIR values corresponding to the smallest (Lu, Yb) and the biggest (La, Ce) RE elements cannot be composed (Figure 1b). We point out that the range of AIR values will depend on two factors: the size of a set of RE elements that is used for HE combination generation and the number of RE elements in the generated HE formulation.

Table 1. List of HE Combinations and Their Relevance to Single-Rare-Earth Nd<sub>4</sub>Al<sub>2</sub>O<sub>9</sub>, Gd<sub>4</sub>Al<sub>2</sub>O<sub>9</sub>, Tb<sub>4</sub>Al<sub>2</sub>O<sub>9</sub>, and Y<sub>4</sub>Al<sub>2</sub>O<sub>9</sub> Compounds<sup>a</sup>

	,			
RE =	Y group (i.r. = 0.9000 ± 0.0025)	Tb group (i.r. = $0.9230 \pm 0.0025$ )	Gd group (i.r. = 0.9380 ± 0.0025)	Nd group (i.r. = 0.9830 ± 0.0025)
HE combinations			(Y,La,Pr,Ho,Yb)AM	
			(Y,La,Sm,Gd,Lu)AM	
			(Y,Ce,Pr,Tb,Yb)AM	
			(Y,Ce,Pr,Ho,Er)AM	
		(Y,Ce,Eu,Er,Yb)AM	(Y,Nd,Sm,Eu,Ho)AM	
		(Y,Pr,Tb,Dy,Er)AM	(Y,Nd,Sm,Gd,Dy)AM	
		(Y,Nd,Sm,Dy,Lu)AM	(Y,Nd,Eu,Gd,Tb)AM	
	(Y,Sm,Dy,Yb,Lu)AM	(Y,Nd,Eu,Tb,Lu)AM	(La,Pr,Gd,Yb,Lu)AM	
	(Y,Eu,Tb,Yb,Lu)AM	(La,Tb,Ho,Er,Yb)AM	(La,Nd,Eu,Yb,Lu)AM	
	(Y,Eu,Ho,Er,Lu)AM	(Ce,Eu,Ho,Er,Yb)AM	(La,Nd,Tb,Er,Lu)AM	
	(Y,Gd,Dy,Er,Lu)AM	(Ce, Tb, Dy, Ho, Yb)AM	(La,Nd,Dy,Ho,Lu)AM	(Y,La,Ce,Pr,Nd)AM
	(Sm,Tb,Er,Yb,Lu)AM	(Pr,Nd,Dy,Yb,Lu)AM	(La,Sm,Gd,Ho,Lu)AM	(La,Ce,Pr,Nd,Ho)AM
	(Sm,Dy,Ho,Yb,Lu)AM	(Pr,Sm,Gd,Yb,Lu)AM	(La,Eu,Gd,Dy,Lu)AM	
	(Eu,Tb,Ho,Yb,Lu)AM	(Pr,Tb,Dy,Ho,Er)AM	(Ce,Pr,Gd,Er,Lu)AM	
		(Nd,Sm,Tb,Er,Lu)AM	(Ce,Nd,Eu,Er,Lu)AM	
		(Nd,Sm,Dy,Ho,Lu)AM	(Ce,Nd,Gd,Er,Yb)AM	
		(Nd,Eu,Tb,Ho,Lu)AM	(Ce,Nd,Tb,Dy,Lu)AM	
		(Sm,Eu,Gd,Dy,Lu)AM	(Ce,Sm,Gd,Tb,Lu)AM	
			(Pr,Nd,Sm,Er,Yb)AM	
			(Pr,Nd,Eu,Ho,Yb)AM	
			(Pr,Nd,Gd,Dy,Yb)AM	
			(Nd,Sm,Eu,Dy,Er)AM	

<sup>&</sup>lt;sup>a</sup>The compositions selected for experimental investigation are shown in bold and italicized.

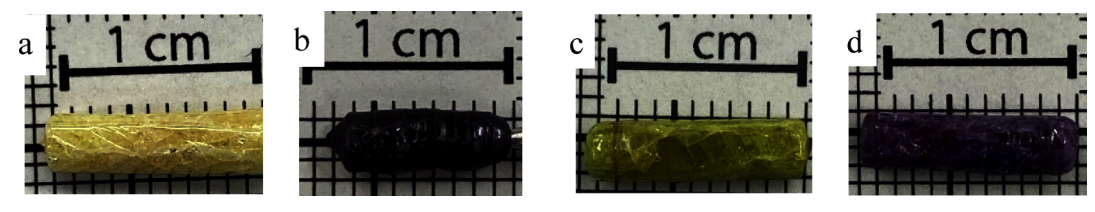


**Figure 2.** Randomly selected representative crystals of the (a) Y group, (b) Nd group, (c) Tb group, and (d) Gd group. (a) (Y,Sm,Dy,Yb,Lu)AM, (b) (Y,La,Ce,Pr,Nd)AM, (c) (Pr,Sm,Gd,Yb,Lu)AM, (d) (Nd,Sm,Eu,Dy,Er)AM.

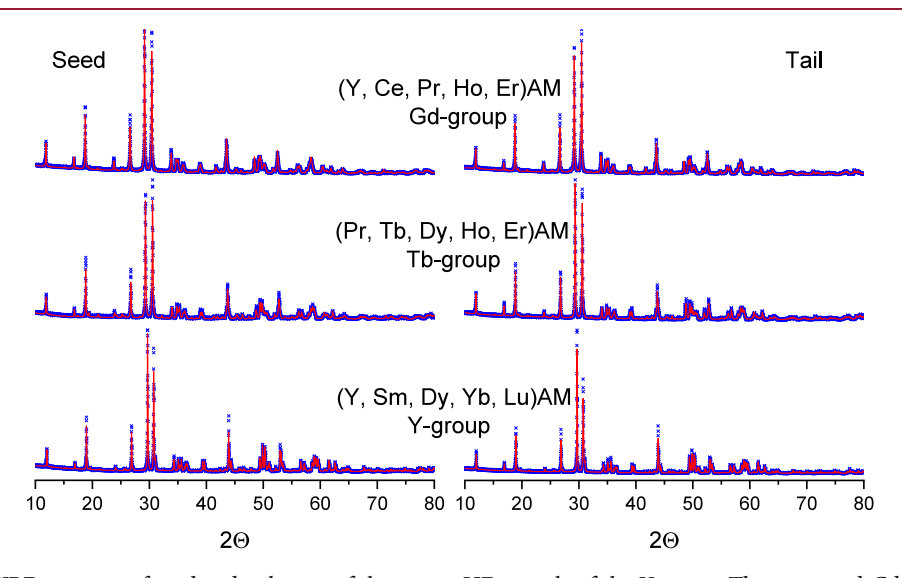


Figure 3. Examples of XRD patterns of seed and tail parts of the grown HE crystals of the Y group, Tb group, and Gd group (indicated). Red lines correspond to the Rietveld refined profiles.  $Y_4Al_2O_9$  (ICSD #252973),  $Gd_4Al_2O_9$  (ICDD #04–010–3647), and  $Tb_4Al_2O_9$  (ICSD #164882) were used as references.

A larger number of elements in an HE formulation (more than five) leads to a narrower range of the AIR values.

For further investigation, we selected only the HE combinations where the AIR value deviation from the ionic

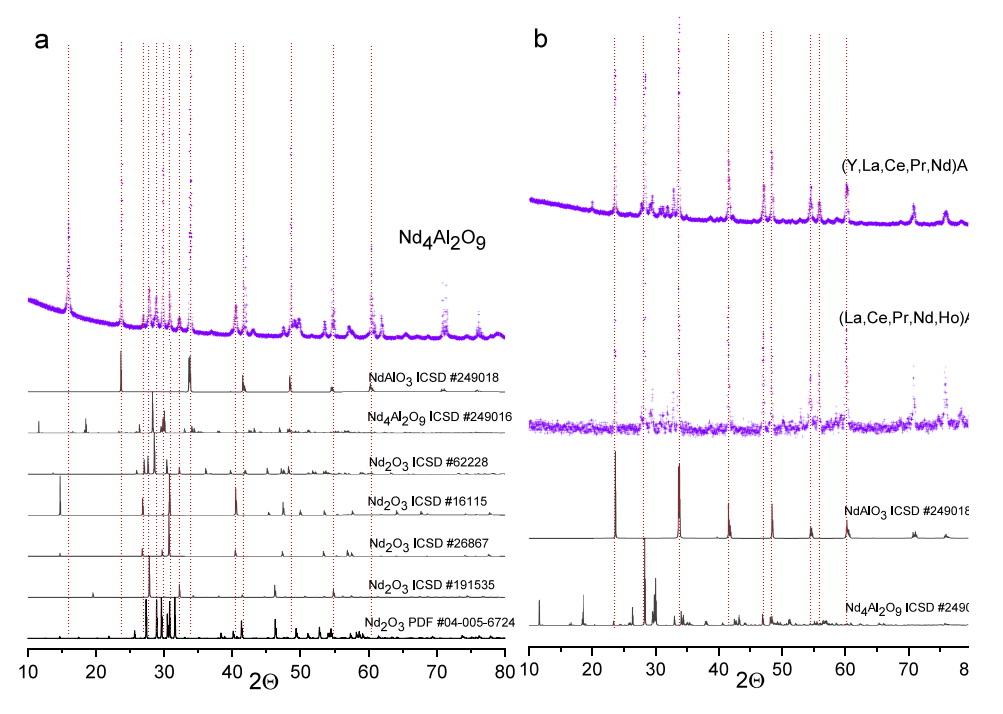


Figure 4. XRD patterns of the  $Nd_4Al_2O_9$  (a) and HE crystals of the Nd group (b). The references for  $NdAlO_3$ ,  $Nd_4Al_2O_9$ , and polymorphous forms of  $Nd_2O_3$  are shown.

radius of Nd (i.r. = 0.983 Å), Gd (i.r. = 0.938 Å), Tb (i.r. = 0.923 Å), and Y (i.r. = 0.9 Å) was less than 0.0025 Å. The selected compositions were arranged into four groups in Table 1: Y group, Nd group, Tb group, and Gd group, based on their relevance to single-rare-earth  $Nd_4Al_2O_9$ ,  $Gd_4Al_2O_9$ ,  $Tb_4Al_2O_9$ , and  $Y_4Al_2O_9$ . As seen in Figure 1b, the selected AIR values cover the whole range of the HE combination distribution.

Finally, two-five HE compositions were randomly selected from each group for further growth experiments and investigation. This random selection was necessary for two reasons. First, the number of HE combinations in some groups was too large to grow all of them. Second, as the AIR values are similar within each group, these HE compositions can be considered equivalent. We expect that the AIR value will play an important role in phase formation rather than the nature of the elements forming the HE composition.

Crystal Growth. Examples of the grown crystals are shown in Figure 2, and the images of all grown crystals and their cross sections of seed and tail sides are shown in Table ST2. Effective control over the crystal diameter, crystal shape, and size of the molten zone was successfully achieved across all compounds from the Y, Gd, and Tb groups despite the complex composition of the melt. The HE compounds of the Y group, Tb group, and Gd group demonstrated the same behavior during growth as their single-rare-earth counterparts, Y<sub>4</sub>Al<sub>2</sub>O<sub>9</sub>, Tb<sub>4</sub>Al<sub>2</sub>O<sub>9</sub>, and Gd<sub>4</sub>Al<sub>2</sub>O<sub>9</sub>. In contrast, challenges were encountered in controlling the molten zone during the growth of Nd<sub>4</sub>Al<sub>2</sub>O<sub>9</sub> and other compounds from the Nd group, leading to inconsistencies in crystal shape, diameter, and unstable melt meniscus (Figure 2b). We attribute these difficulties to the incongruent solidification of the Nd-group compounds. All grown crystals were full of cracks after cooling to room temperature (Table ST2).<sup>19</sup>

**X-ray Diffraction.** XRD was used to examine the phase formation. Since the crystals were grown via directional

solidification from the melt, we can expect some compositional variation and, as a result, different cell parameters between the seed and tail sides due to the segregation effect. Examples of XRD patterns for seed and tail sides of grown crystals of the Y, Tb, and Gd groups are shown in Figure 3, while the XRD patterns of all crystals are listed in Figures S2—S4

The reflections corresponding to the main RE<sub>4</sub>Al<sub>2</sub>O<sub>9</sub> phase were observed in the XRD patterns of the Y-group crystals. In addition to the main phase, minor reflections of the secondary REAlO<sub>3</sub> phase were found in the XRD patterns of the Tb- and Gd-group crystals. Specifically, these crystals from the Tb group are (Pr,Sm,Gd,Yb,Lu)AM (tail side), (Nd,Eu,Tb,Ho,Lu)AM (seed side), and (Pr,Tb,Dy,Ho,Er)-AM) (seed and tail sides). The crystals from the Gd group are (La,Sm,Gd,Ho,Lu)AM (seed and tail sides), (Y,Ce,Pr,Ho,Er)-AM (seed and tail sides), and (Nd,Sm,Eu,Dy,Er)AM (seed and tail sides). The fraction of the secondary perovskite phase determined from the Rietveld refinement is less than 2 wt % for the Tb group and less than 8 wt % for the Gd group. For those crystals where the secondary phase is detected only on one side, we assume that its fraction on the other side is below the XRD detection limit. We must note that identification of the REAlO<sub>3</sub> phase in these compounds is challenging due to overlapping reflections between the two phases, REAlO3 and RE<sub>4</sub>Al<sub>2</sub>O<sub>9</sub>. The Rietveld refinement was performed using GSAS-II software to find the cell parameters of the HE compounds of Y, Gd, and Tb groups. The refinement error did not exceed 8%, all results are listed in Table ST1.

Phase formation of the HE compounds of the Nd group is similar to each other and to that of single-rare-earth Nd<sub>4</sub>Al<sub>2</sub>O<sub>9</sub>. The Nd-group crystals cracked and crumbled soon after the growth, so we measured XRD of whole crystals rather than only the seed and tail parts as opposed to other crystals. Rietveld refinement was not applied to Nd-group samples due to the large amounts of secondary phases. In

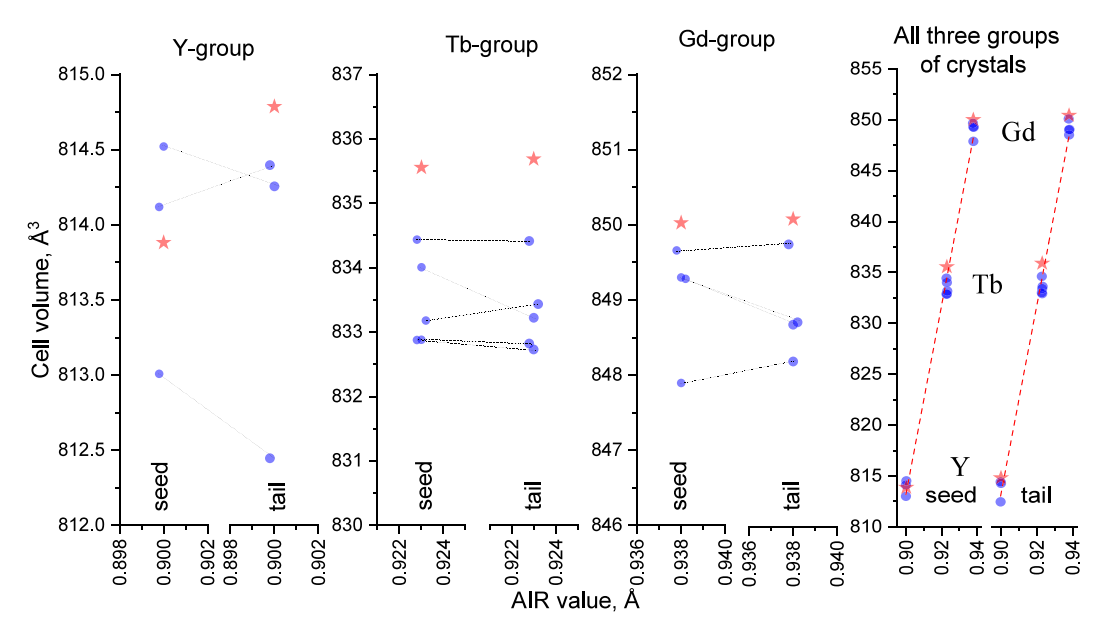


Figure 5. Correlation between AIR values of grown HE compounds and their unit cell volumes for seed and tail parts of the crystal (indicated). The relevance to the Y, Tb, and Gd groups is indicated. Red stars correspond to the single-rare-earth  $Y_4Al_2O_9$ ,  $Tb_4Al_2O_9$ , and  $Gd_4Al_2O_9$ . Blue circles correspond to HE compounds. Dashed lines connect data points for the seed and tail sides of the same crystals. Error bars were not included in the plot to keep it easy for readers.

addition to the monoclinic phase, intense reflections of secondary phases are registered in the XRD patterns for both single-rare-earth Nd<sub>4</sub>Al<sub>2</sub>O<sub>9</sub> and HE compounds of the Nd group (Figure 4). As we noted before, Nd<sub>4</sub>Al<sub>2</sub>O<sub>9</sub> melts incongruently and decomposes into perovskite (NdAlO<sub>3</sub>) and  $Nd_2O_3$  phases upon crystallization.<sup>39</sup> However, in addition to NdAlO<sub>3</sub> and Nd<sub>2</sub>O<sub>3</sub>, the reflections of the desired monoclinic phase were present in the XRD patterns for the grown Nd<sub>4</sub>Al<sub>2</sub>O<sub>9</sub> crystal (Figure 4a). It is known that preservation of the Nd<sub>4</sub>Al<sub>2</sub>O<sub>9</sub> phase is possible during melt solidification when a relatively high cooling rate is used.<sup>39</sup> In our growth experiments, we used a relatively fast cooling rate to favor monoclinic phase preservation. Most single-component RE<sub>2</sub>O<sub>3</sub> compounds exhibit polymorphism, which makes it challenging to identify their reflections in the XRD patterns of HE compounds.<sup>43</sup> We added the reference patterns for Nd<sub>2</sub>O<sub>3</sub> isomorphous phases in Figure 4a to demonstrate their contribution to the XRD pattern of the Nd<sub>4</sub>Al<sub>2</sub>O<sub>9</sub> crystal. In the case of HE compounds of the Nd group, the reflections unmatched to Nd<sub>4</sub>Al<sub>2</sub>O<sub>9</sub> and NdAlO<sub>3</sub> reference patterns correspond to various polymorphous forms of RE2O3 forming the HE compositions.

The overall tendency of secondary phase formation strongly correlates with the AIR value of HE compounds. Our XRD measurements confirmed that the HE compounds of the Y group are single-phase, while the secondary REAlO<sub>3</sub> perovskite phase is registered for HE compounds of the Tb and Gd groups in addition to the main monoclinic phase. Single rareearth monoclinic aluminates formed by smaller RE (i.r. = 0.861–0.947 Å) like Y<sub>4</sub>Al<sub>2</sub>O<sub>9</sub>, Lu<sub>4</sub>Al<sub>2</sub>O<sub>9</sub>, Er<sub>4</sub>Al<sub>2</sub>O<sub>9</sub>, Yb<sub>4</sub>Al<sub>2</sub>O<sub>9</sub>, and Tb<sub>4</sub>Al<sub>2</sub>O<sub>9</sub> tend to crystallize in a single monoclinic phase. Single rare-earth aluminates formed by larger RE (i.r. = 0.958–1.032 Å) like elements such as Nd<sub>4</sub>Al<sub>2</sub>O<sub>9</sub>, Sm<sub>4</sub>Al<sub>2</sub>O<sub>9</sub>, La<sub>4</sub>Al<sub>2</sub>O<sub>9</sub>, Pr<sub>4</sub>Al<sub>2</sub>O<sub>9</sub>, and Ce<sub>4</sub>Al<sub>2</sub>O<sub>9</sub> have difficulty crystallizing from the melt in a single phase and tend to form a secondary perovskite phase. <sup>18,45</sup> Our results on HE compounds agree with the phase formation trend observed in the single-rare-

earth monoclinic aluminates. The value of AIR increases from 0.923 to 0.938 Å when moving from the Tb group to the Gd group. The stability of the perovskite phase is known to increase with ionic radii. Thus, the Gd group should have a higher concentration of the secondary phase, which is confirmed by our XRD measurements (2 wt % for the Tb group and less than 8 wt % for the Gd group). To suppress the formation of the secondary perovskite phase during melt growth, either the HE compounds with smaller AIR values should be preferred or bigger ions, like La, Pr, Ce, Sm, and Nd, should be minimized in the composition formulation.

A correlation between the AIR values of the HE compounds from Y, Tb, and Gd groups and their unit cell volumes from the Rietveld refinement is shown in Figure 5. The unit cell volumes for HE compounds are similar to their corresponding single-rare-earth (Y<sub>4</sub>Al<sub>2</sub>O<sub>9</sub>, Tb<sub>4</sub>Al<sub>2</sub>O<sub>9</sub>, and Gd<sub>4</sub>Al<sub>2</sub>O<sub>9</sub>) compounds, confirming their structural similarity. The linear correlation between AIR value and cell volume of the HE compounds of the Y group, Gd group, and Tb group is registered. A similar correlation between the AIR value and cell volume was observed for other HE RE monoclinic aluminates.<sup>14</sup> We can conclude that the single-rare-earth compounds with ionic radii that are similar to the AIR values of HE compositions can be used as a reference for predicting their structural parameters. This feature can be useful in the development of HE luminescent materials where dopant emission, like Ce3+ or Eu2+, is sensitive to the crystalline surroundings.<sup>47</sup> Small differences in the refined unit cell volumes between the seed and tail sides are due to the minor differences in the position of XRD reflections and, as a result, cell parameters (Table ST1). The REAlO3 phase formation in the seed and tail sides or negligible axial segregation of RE elements can affect the RE ions ratio in the monoclinic structure and, as a result, cell parameters. As mentioned earlier, the RE ions can occupy 6- and 7-fold coordinated sites in the RE<sub>4</sub>Al<sub>2</sub>O<sub>9</sub> crystal structure where they have different ionic radii. Preferable occupation of 6- or 7-fold sites by some

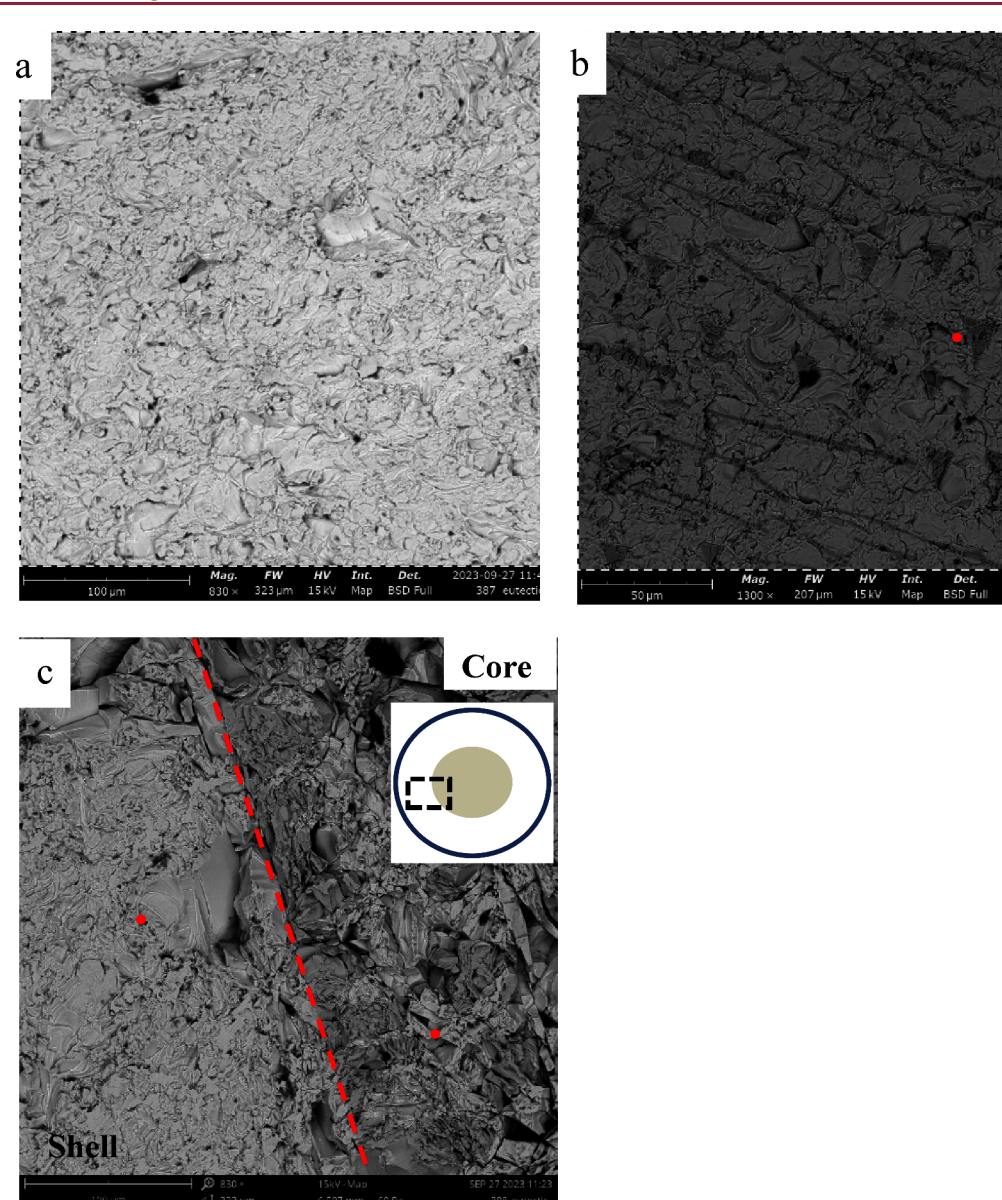


Figure 6. Examples of typical microstructures of the investigated crystals. (a) Uniform microstructure without inclusions in (Ce,Tb,Dy,Ho,Yb)-AM of the Y group. (b) Eutectic dot- and rod-like inclusions in (Nd,Eu,Tb,Ho,Lu)AM of the Tb group. (c) Core-like structure in (Nd,Sm,Eu,Dy,Er)AM of the Gd group; the dashed line corresponds to the core—shell interface. The inset represents the area in the crystal cross section from which the image was taken from. The red circles represent the points that are used for the EDS scans.

RE ions can result in nonuniform distribution between the sites affecting the cell parameter values. Differences in our cell parameters between the seed and tail sides (Figure 5) can be due to the preferred site occupation. The distribution of cations between different sites is not unique and was investigated for different compounds. As, an example, the preferred occupation of RE ions between different sites was shown in  $(Lu_{1-x}Y_x)_2SiO_5$  single crystals with different Lu/Y ratios. It was found that  $Y^{3+}$  prefers to occupy the 7-fold sites, while  $Lu^{3+}$  prevails to be in 6-fold sites in  $(Lu_{1-x}Y_x)_2SiO_5$ .

Scanning Electron Microscopy and Energy Dispersive X-ray Spectroscopy. We conducted SEM and EDS measurements to investigate the microstructure and radial segregation of cations in the seed and tail sides of the crystals. The overview SEM images representing the entire diameter of the crystal were obtained by stitching the sectional SEM

images of the crystal cross-section. The SEM images and EDS plots for all samples are shown in Figures S5–S19. Uniform radial distributions of elements are registered in the seed and tail sides of the EDS profiles in all crystals. The EDS profiles are noisy because of the brittleness of the crystals, which leads to a rough surface and difficulty in sample preparation.

Pulling rate is known to be the most important parameter affecting the axial and radial element distribution for various systems, including solid-state solutions and doped crystals grown by the  $\mu$ -PD method. The elemental segregation will also depend on the melt composition and the nature of the crystalline material and dopants. In our growth experiments, we used a pulling rate of 0.15 mm/min, which is considered to be relatively fast given the complex chemical composition of the melts. A faster pulling rate can favor more intense melt flow and a faster solidification rate, leading to more uniform radial element distribution. A similar effect was

Table 2. Elemental Concentrations (Atom %) in the Micro-Inclusions, Core, and Matrix for (Nd,Eu,Tb,Ho,Lu)AM and (Nd,Sm,Eu,Dy,Er)AM Crystals Obtained from EDS Scans<sup>a</sup>

(Nd,Eu,Tb,Ho,Lu)AM				(Nd,Sm,Eu,Dy,Er)AM			
matrix (monoclinic phase)		inclusion (perovskite phase)		matrix (monoclinic phase)		core (perovskite phase)	
Nd	3.66	Nd	4.63	Nd	3.13	Nd	3.69
Eu	3.21	Eu	3.09	Sm	3.52	Sm	3.66
Tb	3.61	Tb	2.52	Eu	3.06	Eu	3.08
Но	3.63	Но	2.03	Dy	4.40	Dy	2.08
Lu	2.96	Lu	0.94	Er	3.56	Er	1.57
Al	8.73	Al	12.24	Al	9.48	Al	13.84
$\Sigma(RE)/Al$	2.0	$\Sigma(RE)/Al$	1.1	$\Sigma(RE)/Al$	1.9	$\Sigma(RE)/Al$	1.0

<sup>a</sup>Data represent the mean values of three measured points.

observed for HE aluminum garnets grown by the  $\mu\text{-PD}$  method.  $^{7}$ 

**Microstructure Investigation.** Examples of microstructures of grown crystals observed in the SEM images are shown in Figure 6. An SEM image of the sample with a uniform microstructure was also included for comparison (Figure 6a). The homogeneous coloration indicates uniform microstructure, fine lines and dark spots are a result of a rough surface and microcracks. The overview SEM images of the cross sections for all other crystals are shown in Figures S5–S19.

After analyzing the microstructure patterns, we identified a correlation between the presence of La, Ce, Pr, Sm, and Nd elements in the formulation and the occurrence of microinclusions in the HE crystals. The higher the fraction of any of these large elements in the composition, the higher the probability of forming microinclusions during growth. The line- and dotlike microinclusions were found for the (Y,Nd,Eu,Tb,Lu)AM, (Pr,Tb,Dy,Ho,Er)AM, (Pr,Sm,Gd,Yb,Lu)AM, and (Nd,Eu,Tb,Ho,Lu)AM crystals of the Tb group and for the (La,Sm,Gd,Ho,Lu)AM and (Y,La,Sm,Gd,Lu)AM crystals of the Gd group (Figure 6b). For the Tb group, except for (Pr,Sm,Gd,Yb,Lu)AM, the concentration of these inclusions is small and they are located close to the outer edge of the crystal. In the case of (Pr, Sm, Gd, Yb, Lu)AM, a large area with a high concentration of dotand line-like inclusions was found in the center of the crystal, similar to the HE compounds of the Gd group. The diameter of this area was ~1 mm. A uniform core-like structure of the same size was also found for the (Nd, Sm, Eu, Dy, Er)AM crystal of the Gd group. The calculated 12 wt % fraction of the perovskite phase based on the diameter of the core and crystal dimensions correlates well with the fraction of the secondary perovskite phase found by XRD (8 wt %). Preferential incorporation of the secondary phase inclusions in the center vs the outer edge of the crystal is likely due to a higher melting point of the HE perovskite phase relative to that of the HE monoclinic phase. In single-RE systems, the relative melting points of the two phases, monoclinic and perovskite, are known to vary across the RE series. 18 Multicomponent HE perovskite phases composed of large ions are expected to have higher melting points compared to the monoclinic phases composed of smaller ions, and, due to strong radial thermal gradients in the  $\mu$ -PD molten zone, <sup>60</sup> they tend to crystallize in the middle of the crystal. A similar effect of some elements raising the melting point and preferably solidifying in the crystal center was observed in μ-PD-grown Yb-doped (Y<sub>0.5</sub>Sc<sub>0.5</sub>)O<sub>3</sub> crystals.<sup>61</sup> In the case of the Y group, microinclusions were not detected by SEM. The SEM images for the crystals of the Nd group are not listed

because the crystals crumbled soon after the growth, as we mentioned before.

Using point EDS scans, we confirmed that the dot-like microinclusions in the (Nd,Eu,Tb,Ho,Lu)AM crystal and the core part in the (Nd,Sm,Eu,Dy,Er)AM crystal, Figure 6b,c, are the REAlO<sub>3</sub> perovskite phase (Table 2). The ratio between the total amounts of RE and Al (RE:Al) for microinclusions and the core is close to one, while the same ratio for the matrix is close to two. These values are close to the  $\Sigma RE:Al$ ratios in REAlO<sub>3</sub> and RE<sub>4</sub>Al<sub>2</sub>O<sub>9</sub>, respectively. This is in agreement with the XRD results, where the secondary perovskite phase was found for these samples. The inclusions have a higher concentration of bigger ions such as Nd or La. We can assume that smaller ions are less likely to form the perovskite phase according to the Goldschmidt factor (for example, 0.95 for LuAlO<sub>3</sub>, Lu being the smallest RE), unlike the larger La and Nd ions, which have a higher tendency to form a perovskite phase.61 The Goldschmidt factor for the largest La ion is 1.01, which is close to the ideal value of 1.00.

Crystal Color. All grown crystals have different colors that correlate with the composition in most cases. This aspect can be used for color prediction and can be useful in the case of optical applications of these materials. Most of the crystals containing Nd in the composition are purple, while Tb in the composition leads to crystals of brown color. The formation of greenish crystals is observed in the case when Pr is one of the elements and Nd, Tb, and Ce are not included in the composition. The presence of pairs, Ce with Pr or Nd with Tb, in the composition results in nearly black crystals. The absence of Ce, Nd, Pr, or Tb in the composition causes yellowish crystals. It is important to note that the black or dark-brown colors are unexpected and do not correspond to the color of the raw oxides used for growth. Raw oxides Tb<sub>2</sub>O<sub>3</sub> and Ce<sub>2</sub>O<sub>3</sub> are yellowish and Pr<sub>2</sub>O<sub>3</sub> has a light-green color. It can be assumed that the deviation in the crystal color is a result of a possible change in the valence state of some rare-earth ions such as Ce, Pr, Tb, or Eu. The possibility of change in oxidation state in the HE rare-earth monoclinic aluminates was demonstrated before.<sup>14</sup>

Recommendations for HE Composition Selection. Our experimental results demonstrate that with an increasing AIR value, the tendency of secondary perovskite phase formation increases. We found that this tendency is a result of increasing the fraction of RE ions with larger ionic radii like La, Pr, Ce, Sm, or Nd in the HE formulation. To demonstrate this effect, we calculated the average number of La, Pr, Ce, Sm, and Nd elements per HE composition for each group in Table 1; it increases from 0.43 for the Y group, 1.29 for the Tb group, 1.95 for the Gd group, and 4 for the Nd group,

similar to the increase of the AIR values in the same series. These correlate with the contributions of RE elements in HE formulations in Figure 1a. A larger AIR value requires that RE ions with bigger ionic radii are included in the formulation.

We can divide the AIR range into three zones: small AIR values (0.861-0.912 Å) where only the single monoclinic phase is observed; middle AIR values (0.912-0.958 Å) where the secondary perovskite phase is observed in addition to the desired monoclinic phase; and big AIR values (0.958-1.032 Å), corresponding to ionic radii of the biggest RE, where the single monoclinic phase is difficult to obtain. The borders between these groups are approximate and are based on the number of possible HE combinations in these ranges. The middle zone represents a range where the highest variety of RE elements can be used to generate HE combinations. This variety leads to a different number of any of the smallest (Y, Lu, Er, Yb, and Ho) and any of the biggest (La, Pr, Ce, Sm, and Nd) RE elements in the HE formulation. The ratio between the number of large and the number of small RE can predict the formation of secondary perovskite phase inclusions. This is illustrated by a couple of examples from the Tb group. (Pr,Sm,Gd,Yb,Lu)AM contains two large ions (Pr and Sm) and two smaller ions (Lu, Yb) and, therefore, has a higher density of microinclusions (Figure S12). (Y,Nd,Eu,Tb,Lu)AM contains one large ion (Nd) and two smaller ions (Y, Lu) and the crystal has a lower density of microinclusions (Figure S10).

The small zone (0.861–0.912 Å) and big zone (0.958–1.032 Å) are represented by the Y group (smaller RE) and the Nd group (bigger RE), respectively (Figure 1). The total number of HE combinations in each zone is small, and those that were investigated had strong correlations of phase formation with their single-rare-earth  $Y_4Al_2O_9$  and  $Nd_4Al_2O_9$  compounds. As a result, we can expect that all HE compounds in these zones will have the same phase formation tendencies as their single-rare-earth counterparts. The total number of HE combinations in the middle zone is too large, and it can be challenging to predict phase formation due to the large diversity of RE elements that can be used for composition formulation.

Considering our results, we can provide a few recommendations on how to stabilize the primary monoclinic phase and avoid secondary perovskite phase formation when selecting an HE combination for crystal growth from the melt. The fraction of RE ions with bigger ionic radii (La, Pr, Ce, Sm, Nd) in the HE composition should be minimized, and only the HE combinations with the smallest AIR values corresponding to the small zone (0.861-0.912 Å) should be chosen. We can not provide the exact threshold AIR values because those chosen for our investigation, Y, Tb, Gd, and Nd groups, are discrete, and they do not represent the continuous distribution of AIR values in the range of RE ionic radii. Several strategies can be considered to minimize the presence of La, Pr, Ce, Sm, and Nd in HE formulations. First, the formulation can be adjusted to use nonequimolar ratios of elements to minimize the fraction of larger RE ions. By doing that, the overall number of HE combinations was not drastically reduced. Second, with an increasing number of RE elements (beyond the five discussed here) in the HE formulation, the fraction of RE elements with bigger ionic radii will be diluted.

#### CONCLUSIONS

We applied a combinatorial approach and the AIR concept to design multirare-earth compounds in the  $RE_4Al_2O_9$  aluminum monoclinic system. Using equimolar ratios of five RE elements from this list, Y, La, Ce, Pr, Nd, Sm, Eu, Gd, Tb, Dy, Ho, Er, Yb, and Lu, we generated 2002 unique HE combinations. The highest number of HE combinations was observed for the AIR values equal to the ionic radii of Tb, Gd, and Eu. The smallest number of HE combinations was observed for the AIR values corresponding to the smallest (Y, Er) and biggest (Pr, Nd) RE elements. The HE combinations with AIR values equal to that of RE element in single-rare-earth  $RE_4Al_2O_9$ :  $Nd_4Al_2O_9$  (Nd group),  $Gd_4Al_2O_9$  (Gd group),  $Tb_4Al_2O_9$  (Tb group), and  $Y_4Al_2O_9$  (Y group) were selected for experimental investigation.

We used the  $\mu$ -PD method to grow a few randomly selected representative compositions and investigated their phase formation, microstructure, and elemental segregation. We found that phase formation in these groups is similar to that of their single-rare-earth counterparts: Nd<sub>4</sub>Al<sub>2</sub>O<sub>9</sub>, Gd<sub>4</sub>Al<sub>2</sub>O<sub>9</sub>, Tb<sub>4</sub>Al<sub>2</sub>O<sub>9</sub>, and Y<sub>4</sub>Al<sub>2</sub>O<sub>9</sub>. The single monoclinic phase and uniform microstructure were found for the Y group. Incongruent solidification from the melt was confirmed for the Nd group. Dot-, line-, and core-like inclusions corresponding to a REAlO<sub>3</sub> secondary phase were found for HE compounds of the Tb group and Gd group. The dot- and line-like inclusions are mostly located close to the center in the crystals of the Gd group, while in the case of the Tb group, they are located close to the outer edges and center of the crystal. The concentration of inclusions is the highest in the Gd group. We assumed that this results from a higher fraction of larger ions such as La, Pr, Ce, Sm, or Nd in the HE formulation. The average number of La, Pr, Ce, Sm, and Nd elements per HE composition was found to be 0.43 for the Y group, 1.29 for the Tb group, 1.95 for the Gd group, and 4 for the Nd group, similar to the increase in the AIR values. Negligible deviations in cell parameters between the seed and tail sides of the crystals of the Y group, Tb group, and Gd group may originate from minor axial segregation of the RE elements.

We also provided some recommendations regarding HE composition selection to grow crystals with a single monoclinic phase. They include minimizing the number of large elements like La, Pr, Ce, Sm, or Nd in a HE formulation by designing nonequimolar compositions and increasing the total number of RE elements in a HE formulation above five that was studied in this work. The AIR value of a HE formulation should be selected from the small zone (0.861–0.912 Å). The borders are approximate and are based on our grouping of AIR values in three zones.

#### ASSOCIATED CONTENT

# **Supporting Information**

ı

The Supporting Information is available free of charge at https://pubs.acs.org/doi/10.1021/acs.cgd.4c00633.

Unit cell structure of RE<sub>4</sub>Al<sub>2</sub>O<sub>9</sub> and interconnection of REO<sub>6</sub>, REO<sub>7</sub>, and Al<sub>2</sub>O<sub>7</sub>polyhedra in RE<sub>4</sub>Al<sub>2</sub>O<sub>9</sub> structure; list of selected HE compositions divided into four groups Y, Gd, Nd, and Tb based on their AIR values; composition of the grown crystals and their photos; XRD patterns of the grown crystals of the Y group; XRD patterns of the grown crystals of the Tb

group; XRD patterns of the grown crystals of the Gd group; stitched SEM images of seed and tail sides of YAM crystals coupled with EDS scans; stitched SEM images of seed and tail sides of (Y,Sm,Dy,Yb,Lu)AM crystals coupled with EDS scans; stitched SEM images of seed and tail sides of (Y, Eu, Tb, Yb, Lu)AM crystals coupled with EDS scans; stitched SEM images of seed and tail sides of (Sm, Dy, Ho, Yb, Lu)AM crystals coupled with EDS scans; stitched SEM images of seed and tail sides of TbAM crystals coupled with EDS scans; stitched SEM images of seed and tail sides of (Y, Nd, Eu, Tb, Lu)AM crystals coupled with EDS scans; stitched SEM images of seed and tail sides of (Ce, Tb, Dy, Ho, Yb)AM crystals coupled with EDS scans; stitched SEM images of seed and tail sides of (Pr, Sm, Gd, Yb, Lu)AM crystals coupled with EDS scans; stitched SEM images of seed and tail sides of (Pr, Tb, Dy, Ho, Er)AM crystals coupled with EDS scans; stitched SEM images of seed and tail sides of (Nd, Eu, Tb, Ho, Lu)AM crystals coupled with EDS scans; stitched SEM images of seed and tail sides of GdAM crystals coupled with EDS scans; stitched SEM images of seed and tail sides of (Y, La, Sm, Gd, Lu)AM crystals coupled with EDS scans; stitched SEM images of seed and tail sides of (Y, Ce, Pr, Ho, Er)AM crystals coupled with EDS scans; stitched SEM images of seed and tail sides of (La, Sm, Gd, Ho, Lu)AM crystals coupled with EDS scans; and stitched SEM images of seed and tail sides of (Nd, Sm, Eu, Dy, Er)AM crystals coupled with EDS scans (PDF)

# AUTHOR INFORMATION

### **Corresponding Author**

Yauhen Tratsiak — Scintillation Materials Research Center, University of Tennessee, Knoxville, Tennessee 37996, United States; orcid.org/0000-0002-1432-1054; Email: ytratsia@utk.edu

#### Authors

Bethany Claes – Scintillation Materials Research Center and Department of Materials Science and Engineering, University of Tennessee, Knoxville, Tennessee 37996, United States

Charles L. Melcher – Scintillation Materials Research Center, Department of Materials Science and Engineering, and Department of Nuclear Engineering, University of Tennessee, Knoxville, Tennessee 37996, United States

Mariya Zhuravleva — Scintillation Materials Research Center and Department of Materials Science and Engineering, University of Tennessee, Knoxville, Tennessee 37996, United States

Complete contact information is available at: https://pubs.acs.org/10.1021/acs.cgd.4c00633

## **Author Contributions**

The manuscript was written through contributions of all authors. All authors have given approval to the final version of the manuscript.

#### **Funding**

This project was supported by the National Science Foundation (DMR 1846935).

#### Notes

The authors declare no competing financial interest.

## ACKNOWLEDGMENTS

This project was supported by the National Science Foundation (DMR 1846935). Powder X-ray diffraction was performed at the Institute for Advanced Materials and Manufacturing (IAMM) Diffraction Facility, located at the University of Tennessee, Knoxville.

#### ABBREVIATIONS

RE, rare-earth element; HE, high entropy; AIR, average ionic radius

# REFERENCES

- (1) Zhang, X.; Xu, W.; Zhang, J.; Huang, P.; Qi, X. High-Entropy Oxide Glasses TiO2-Ta2O5-Nb2O5-WO3-MOx (M = La/Sm/Eu/Tb/Dy) with High Refractive Index. *J. Non Cryst. Solids* **2022**, 597, No. 121862.
- (2) Pianassola, M.; Chakoumakos, B. C.; Melcher, C. L.; Zhuravleva, M. Crystal Growth and Phase Formation of High-Entropy Rare-Earth Aluminum Perovskites. *Cryst. Growth Des* **2023**, 23 (1), 480–488.
- (3) Han, W.; Ye, Y.; Lu, K.; Wu, Y.; Wang, H.; Huang, Z.; Qi, J.; Lu, T. High-Entropy Transparent (Y0.2La0.2Gd0.2Yb0.2Dy0.2)-2Zr2O7 Ceramics as Novel Phosphor Materials with Multi-Wavelength Excitation and Emission Properties. *J. Eur. Ceram Soc.* 2023, 43 (1), 143–149.
- (4) Zhang, G.; Wu, Y. High-entropy Transparent Ceramics: Review of Potential Candidates and Recently Studied Cases. *Int. J. Appl. Ceram Technol.* **2022**, *19* (2), 644–672.
- (5) Corey, Z. J.; Lu, P.; Zhang, G.; Sharma, Y.; Rutherford, B. X.; Dhole, S.; Roy, P.; Wang, Z.; Wu, Y.; Wang, H.; Chen, A.; Jia, Q. Structural and Optical Properties of High Entropy (La,Lu,Y,Gd,Ce)-AlO 3 Perovskite Thin Films. *Advanced Science* **2022**, *9* (29), 2202671.
- (6) Mao, H.; Wang, L.; Li, J.; Jiang, X.; Xue, S.; Li, M.; Zhu, J.; Fan, B.; Xu, T.; Shao, G.; Xu, H.; Wang, H.; Zhang, R.; Lu, H. High-Entropy Cs(Pb <sub>1/3</sub> Mn <sub>1/3</sub> Ni <sub>1/3</sub>)Br <sub>3</sub> Perovskite Nanocrystals Prepared by High Energy Ball Milling and Their Luminescence Properties. *Particle & Particle Systems Characterization* **2022**, 39 (9), 2200073
- (7) Pianassola, M.; Loveday, M.; Chakoumakos, B. C.; Koschan, M.; Melcher, C. L.; Zhuravleva, M. Crystal Growth and Elemental Homogeneity of the Multicomponent Rare-Earth Garnet (Lu1/6Y1/6Ho1/6Dy1/6Tb1/6Gd1/6)3Al5O12. *Cryst. Growth Des* **2020**, 20 (10), 6769–6776.
- (8) Ying, T.; Yu, T.; Qi, Y.; Chen, X.; Hosono, H. High Entropy van Der Waals Materials. Advanced Science 2022, 9 (30), 2203219.
- (9) Wang, J.; Cui, Y.; Wang, Q.; Wang, K.; Huang, X.; Stenzel, D.; Sarkar, A.; Azmi, R.; Bergfeldt, T.; Bhattacharya, S. S.; Kruk, R.; Hahn, H.; Schweidler, S.; Brezesinski, T.; Breitung, B. Lithium Containing Layered High Entropy Oxide Structures. *Sci. Rep* **2020**, *10* (1), 1–13.
- (10) Zhang, R. Z.; Reece, M. J. Review of High Entropy Ceramics: Design, Synthesis, Structure and Properties. *Journal of Materials Chemistry A* **2019**, *7*, 22148–22162.
- (11) Li, H.; Zhu, H.; Zhang, S.; Zhang, N.; Du, M.; Chai, Y. Nano High-Entropy Materials: Synthesis Strategies and Catalytic Applications. *Small Struct* **2020**, *1* (2), 2000033.
- (12) Xiang, H.; Xing, Y.; Dai, F. zhi; Wang, H.; Su, L.; Miao, L.; Zhang, G.; Wang, Y.; Qi, X.; Yao, L.; Wang, H.; Zhao, B.; Li, J.; Zhou, Y. High-Entropy Ceramics: Present Status, Challenges, and a Look Forward. *J. Adv. Ceram.* **2021**, *10*, 385–441.
- (13) Yanagida, T.; Yamazaki, T. Inorganic Scintillating Materials and Scintillation Detectors. *Proceedings of the Japan Academy, Series B* **2018**, *94* (2), 75–97.
- (14) Pianassola, M.; Loveday, M.; Lalk, R.; Pestovich, K.; Melcher, C. L.; Zhuravleva, M. Crystal Growth and Phase Formation of High-

- Entropy Rare-Earth Monoclinic Aluminates. J. Am. Ceram. Soc. 2023, 106 (11), 7123-7132.
- (15) Pianassola, M.; Stand, L.; Loveday, M.; Chakoumakos, B. C.; Koschan, M.; Melcher, C. L.; Zhuravleva, M. Czochralski Growth and Characterization of the Multicomponent Garnet (Lu1/4Yb1/4Y1/4Gd1/4)3Al5 O12. *Phys. Rev. Mater.* **2021**, *5* (8), No. 083401.
- (16) Markovskyi, A.; Gieszczyk, W.; Bilski, P.; Fedorov, A.; Bartosiewicz, K.; Paprocki, K.; Zorenko, T.; Zorenko, Y. Composition Engineering of Tb3-XGdxAl5-YGayO12:Ce Single Crystals and Their Luminescent, Scintillation and Photoconversion Properties. J. Alloys Compd. 2020, 849, No. 155808.
- (17) Nargelas, S.; Talochka, Y.; Vaitkevičius, A.; Dosovitskiy, G.; Buzanov, O.; Vasil'ev, A.; Malinauskas, T.; Korzhik, M.; Tamulaitis, G. Influence of Matrix Composition and Its Fluctuations on Excitation Relaxation and Emission Spectrum of Ce Ions in (Gdx Y1-x)3Al2Ga3O12:Ce Scintillators. *J. Lumin.* 2022, 242, No. 118590.
- (18) Wu, P.; Pelton, A. D. Coupled Thermodynamic-Phase Diagram Assessment of the Rare Earth Oxide-Aluminium Oxide Binary Systems. *J. Alloys Compd.* **1992**, *179* (1–2), 259–287.
- (19) Zhao, Z.; Xiang, H.; Chen, H.; Dai, F. Z.; Wang, X.; Peng, Z.; Zhou, Y. High-Entropy (Nd0.2Sm0.2Eu0.2Y0.2Yb0.2)4Al2O9 with Good High Temperature Stability, Low Thermal Conductivity, and Anisotropic Thermal Expansivity. *Journal of Advanced Ceramics* **2020**, 9 (5), 595–605.
- (20) Yamane, H.; Ogawara, K.; Omori, M.; Hirai, T. Phase Transition of Rare-Earth Aluminates (RE4Al2O9) and Rare-Earth Gallates (RE4Ga2O9). *J. Am. Ceram. Soc.* **1995**, 78 (9), 2385–2390.
- (21) Yamane, H.; Omori, M.; Okubo, A.; Hirai, T. High-Temperature Phase Transition of Y4Al2O9. *J. Am. Ceram. Soc.* 1993, 76 (9), 2382–2384.
- (22) Gervais, M.; Douy, A. Solid Phase Transformation and Metlting of the Compounds Ln4Al2O9 (Ln Gd, Dy, Y). *Materials Science and Engineering: B* **1996**, 38 (1–2), 118–121.
- (23) Kamada, K.; Yanagida, T.; Pejchal, J.; Nikl, M.; Endo, T.; Tsutumi, K.; Fujimoto, Y.; Fukabori, A.; Yoshikawa, A. Scintillator-Oriented Combinatorial Search in Ce-Doped (Y,Gd)3(Ga,Al)5O12 Multicomponent Garnet Compounds. J. Phys. D Appl. Phys. 2011, 44 (50), 505104.
- (24) Zorenko, Y.; Gorbenko, V.; Zorenko, T.; Sidletskiy, O.; Fedorov, A.; Bilski, P.; Twardak, A. High-Perfomance Ce-Doped Multicomponent Garnet Single Crystalline Film Scintillators. *Phys. Status Solidi RRL* **2015**, 9 (8), 489–493.
- (25) Kaufmann, K.; Maryanovsky, D.; Mellor, W. M.; Zhu, C.; Rosengarten, A. S.; Harrington, T. J.; Oses, C.; Toher, C.; Curtarolo, S.; Vecchio, K. S. Discovery of High-Entropy Ceramics via Machine Learning. NPJ. Comput. Mater. 2020, 6 (1), 1–9.
- (26) Wang, Q.; Velasco, L.; Breitung, B.; Presser, V. High-Entropy Energy Materials in the Age of Big Data: A Critical Guide to Next-Generation Synthesis and Applications. *Adv. Energy Mater.* **2021**, *11* (47), 2102355.
- (27) Gebhardt, T.; Music, D.; Takahashi, T.; Schneider, J. M. Combinatorial Thin Film Materials Science: From Alloy Discovery and Optimization to Alloy Design. *Thin Solid Films* **2012**, *520*, 5491–5499.
- (28) Amis, E. J.; Xiang, X. D.; Zhao, J. C. Combinatorial Materials Science: What's New since Edison? *MRS Bull.* **2002**, 27 (4), 295–300.
- (29) Spiridigliozzi, L.; Ferone, C.; Cioffi, R.; Dell'Agli, G. A Simple and Effective Predictor to Design Novel Fluorite-Structured High Entropy Oxides (HEOs). *Acta Mater.* **2021**, 202, 181–189.
- (30) Teng, Z.; Tan, Y.; Zeng, S.; Meng, Y.; Chen, C.; Han, X.; Zhang, H. Preparation and Phase Evolution of High-Entropy Oxides A2B2O7 with Multiple Elements at A and B Sites. *J. Eur. Ceram Soc.* **2021**, *41* (6), 3614–3620.
- (31) Kuo, C. H.; Wang, A. Y.; Liu, H. Y.; Huang, S. C.; Chen, X. R.; Chi, C. C.; Chang, Y. C.; Lu, M. Y.; Chen, H. Y. A Novel Garnet-Type High-Entropy Oxide as Air-Stable Solid Electrolyte for Li-Ion Batteries. *APL Mater.* **2022**, *10* (12), 121104.

- (32) Chen, D.; Yang, Y.; Chen, C.; Meng, Y.; Zhang, Y.; Zhang, C. Structure and Magnetism of Novel High-Entropy Rare-Earth Iron Garnet Ceramics. *Ceram. Int.* **2023**, 49 (6), 9862–9867.
- (33) Sarkar, A.; Djenadic, R.; Wang, D.; Hein, C.; Kautenburger, R.; Clemens, O.; Hahn, H. Rare Earth and Transition Metal Based Entropy Stabilised Perovskite Type Oxides. *J. Eur. Ceram Soc.* **2018**, 38 (5), 2318–2327.
- (34) Corey, Z. J.; Lu, P.; Zhang, G.; Sharma, Y.; Rutherford, B. X.; Dhole, S.; Roy, P.; Wang, Z.; Wu, Y.; Wang, H.; Chen, A.; Jia, Q. Structural and Optical Properties of High Entropy (La,Lu,Y,Gd,Ce)-AlO 3 Perovskite Thin Films. *Advanced Science* **2022**, 9 (29), 2202671.
- (35) Witte, R.; Sarkar, A.; Velasco, L.; Kruk, R.; Brand, R. A.; Eggert, B.; Ollefs, K.; Weschke, E.; Wende, H.; Hahn, H. Magnetic Properties of Rare-Earth and Transition Metal Based Perovskite Type High Entropy Oxides. *J. Appl. Phys.* **2020**, *127* (18), 185109.
- (36) Corey, Z. J.; Lu, P.; Zhang, G.; Sharma, Y.; Rutherford, B. X.; Dhole, S.; Roy, P.; Wang, Z.; Wu, Y.; Wang, H.; Chen, A.; Jia, Q. Structural and Optical Properties of High Entropy (La,Lu,Y,Gd,Ce)-AlO3 Perovskite Thin Films. *Advanced Science* **2022**, 9 (29), 2202671.
- (37) Fukuda, T.; Chani, V. I. Shaped Crystals: Micro-Pulling-down Technique and Growth. Springer Science & Business Media 2007.
- (38) Yoshikawa, A.; Nikl, M.; Boulon, G.; Fukuda, T. Challenge and Study for Developing of Novel Single Crystalline Optical Materials Using Micro-Pulling-down Method. *Opt Mater.* (*Amst*) **2007**, *30* (1), 6–10.
- (39) COUTURES, J. P. The Al2O3-Nd2O3 Phase Diagram. *J. Am. Ceram. Soc.* **1985**, *68* (3), 105–107.
- (40) Simura, R.; Yamane, H. Crystal Structure of Lutetium Aluminate (LUAM), Lu4Al2O9. *Acta Crystallogr. E Crystallogr. Commun.* **2020**, *76* (5), 752–755.
- (41) Kumar, P.; Singh, D.; Gupta, I.; Singh, S.; Nehra, S.; Kumar, R. Er3+-Doped Y4Al2O9 Nanophosphors for Advance Display Applications: Synthesis, Crystal Chemistry and down Conversion Photoluminescent Investigation. *Mater. Chem. Phys.* **2023**, 301, No. 127610.
- (42) Gasparotto, G.; Tavares, L. S.; Silva, T. C.; Maia, L. J. Q.; Carvalho, J. F. Structural and Spectroscopic Properties of Eu3+Doped Y4Al2O9 Compounds through a Soft Chemical Process. *J. Lumin.* **2018**, 204, 513–519.
- (43) Glushkova, V. B.; Boganov, A. G. Polymorphism of Rare-Earth Sesquioxides. *Bull. Acad. Sci., USSR Div. Chem. Sci.* **1965**, 14 (7), 1101–1107.
- (44) Yamane, H.; Ogawara, K.; Omori, M.; Hirai, T. Phase Transition of Rare-Earth Aluminates (RE4Al2O9) and Rare-Earth Gallates (RE4Ga2O9). *J. Am. Ceram. Soc.* 1995, 78 (9), 2385–2390.
- (45) Dohrup, J.; Høyvald, A.; Mogensen, G.; Jacobsen, C. J. H.; Villadsen, J. Formation of New Compounds Ln  $_4$  Al  $_2$  O  $_9$  in the Ln  $_2$  O  $_3$ Al  $_2$  O  $^3$  System (Ln = La, Pr, Tb). *J. Am. Ceram. Soc.* **1996**, 79 (11), 2959–2960.
- (46) Bartel, C. J.; Sutton, C.; Goldsmith, B. R.; Ouyang, R.; Musgrave, C. B.; Ghiringhelli, L. M.; Scheffler, M. New Tolerance Factor to Predict the Stability of Perovskite Oxides and Halides. *Sci. Adv.* 2019, 5 (2), No. eaav0693.
- (47) Tratsiak, Y.; Trusova, E.; Bokshits, Y.; Korjik, M.; Vaitkevičius, A.; Tamulaitis, G. Garnet-Type Crystallites, Their Isomorphism and Luminescence Properties in Glass Ceramics. *CrystEngComm* **2019**, *21* (4), 687–693.
- (48) Yadav, S. P.; Shinde, S. S.; Bhatt, P.; Meena, S. S.; Rajpure, K. Y. Distribution of Cations in Co1-xMnxFe2O4 Using XRD, Magnetization and Mössbauer Spectroscopy. *J. Alloys Compd.* **2015**, 646, 550-556.
- (49) Kolesov, B. A.; Tanskaya, J. V. Raman Spectra and Cation Distribution in the Lattice of Olivines. *Mater. Res. Bull.* **1996**, *31* (8), 1035–1044.
- (50) Ding, D.; Weng, L.; Yang, J.; Ren, G.; Wu, Y. Influence of Yttrium Content on the Location of Rare Earth Ions in LYSO:Ce Crystals. *J. Solid State Chem.* **2014**, 209, 56–62.

- (51) Uda, S.; Kon, J.; Shimamura, K.; Fukuda, T. Analysis of Ge Distribution in Si1 XGex Single Crystal Fibers by the Micro-Pulling down Method. *J. Cryst. Growth* **1996**, *167* (1–2), 64–73.
- (52) Schäfer, N.; Yamada, T.; Shimamura, K.; Koh, H. J.; Fukuda, T. Growth of SixGe1 x Crystals by the Micro-Pulling-down Method. *J. Cryst. Growth* **1996**, *166* (1–4), 675–679.
- (53) Shim, J. B.; Lee, J. H.; Yoshikawa, A.; Nikl, M.; Yoon, D. H.; Fukuda, T. Growth of Bi4Ge3O12 Single Crystal by the Micro-Pulling-down Method from Bismuth Rich Composition. *J. Cryst. Growth* **2002**, 243 (1), 157–163.
- (54) Ganschow, S.; Klimm, D. Growth of Olivine Single Crystals by the Micro-Pulling-down Method. *Crystal Research and Technology* **2005**, *40* (4–5), 359–362.
- (55) Yoshino, M.; Kotaki, A.; Yokota, Y.; Horiai, T.; Yoshikawa, A. Shape-Controlled Crystal Growth of Y3Al5O12:Ce Single Crystals with Application of Micro-Pulling-Down Method and Mo Crucibles, and Their Scintillation Properties. *Crystals* **2022**, *12* (9), 1215.
- (56) Koh, H. J.; Schäfer, N.; Shimamura, K.; Fukuda, T. Si1 XGex Fiber Crystals with Functionally Variant Composition Grown by Micro-Pulling-down Technique. *J. Cryst. Growth* **1996**, *167* (1–2), 38–44.
- (57) Lan, C. W.; Uda, S.; Fukuda, T. Theoretical Analysis of the Micro-Pulling-down Process for GexSi1-x Fiber Crystal Growth. *J. Cryst. Growth* 1998, 193 (4), 552-562.
- (58) Kononets, V.; Auffray, E.; Dujardin, C.; Gridin, S.; Moretti, F.; Patton, G.; Pauwels, K.; Sidletskiy, O.; Xu, X.; Lebbou, K. Growth of Long Undoped and Ce-Doped LuAG Single Crystal Fibers for Dual Readout Calorimetry. *J. Cryst. Growth* **2016**, 435, 31–36.
- (59) Simura, R.; Yoshikawa, A.; Uda, S. The Radial Distribution of Dopant (Cr, Nd, Yb, or Ce) in Yttrium Aluminum Garnet (Y3Al5O12) Single Crystals Grown by the Micro-Pulling-down Method. *J. Cryst. Growth* **2009**, 311 (23–24), 4763–4769.
- (60) Eckhof, P.; Kalusniak, S.; Brützam, M.; Tanaka, H.; Guguschev, C.; Ganschow, S.; Hülshoff, L.; Wegener, P.; Kränkel, C.; Uvarova, A.; Arlt, I. Growth, Characterization, and Efficient Laser Operation of Czochralski- and Micro-Pulling-down-Grown Yb<sup>3&#x002B</sup>; YScO<sub>3</sub> Mixed Sesquioxides. *Optical Materials Express* **2024**, *14* (2), 304–318.
- (61) Bondar, I. A.; Mezentseva, L. P. Single Crystals of Rare-Earth Oxides: Constitution and Properties. *Progress in Crystal Growth and Characterization* **1988**, *16* (C), 81–141.